ACS APPLIED MATERIALS & INTERFACES

www.acsami.org Research Article

Efficient Electrochemical Lead Detection by a Histidine-Grafted Metal–Organic Framework MOF-808 Electrode Material

Sherman Lesly Zambou Jiokeng,* Tobie J. Matemb Ma Ntep, Marcus N. A. Fetzer, Till Strothmann, Cyrille G. Fotsop, Ignas Kenfack Tonle, and Christoph Janiak*

Cite This: *ACS Appl. Mater. Interfaces* 2024, 16, 2509−2521 Read Online

ABSTRACT: As the excessive presence of heavy metals in the environment significantly affects human health, it becomes necessary to develop efficient, selective, and sensitive methods for their detection. In this study, a novel electrochemical sensor for the detection of Pb^{2+} ions is described. The proposed sensor is based on a glassy carbon electrode (GCE) modified by a thin film of histidine-grafted metal−organic framework (MOF-808-His). The MOF-808 was obtained solvothermally, and then postsynthetically modified by substituting the coordinated acetate with histidinate. By electrochemistry, the MOF-808-His-modified GCE demonstrated high charge selectivity, while electrochemical impedance spectroscopy (EIS) and kinetic studies gave a lower charge transfer resistance (4196 Ω) and a better standard heterogeneous electron transfer rate constant (1.80×10^{-5} cm s^{-1}) on MOF-808-modified GCE. These results indicated a swift and direct electron transfer rate from $[Fe(CN)_6]^{3-/4-}$ to the electrode surface. Using square wave anodic stripping voltammetry (SWASV), the rapid and highly sensitive determination of Pb^{2+} was achieved on MOF-808-His-modified GCE. By optimizing the accumulation-detection parameters including pH of the detection medium, deposition time and potential, and concentration, a remarkable limit of detection (LoD, based on a signal-to-noise ratio of 3) of ($1.12 \times 10^{-10} \pm 0.10 \times 10^{-10}$) mol L^{-1} was obtained, with a sensitivity of (9.6 ± 0.1) μA L μmol^{-1}. After interference and stability studies, the MOF-808-His-modified GCE was applied to the detection of Pb^{2+} in a tap water sample with a concentration of 10 μmol L^{-1} Pb^{2+}.

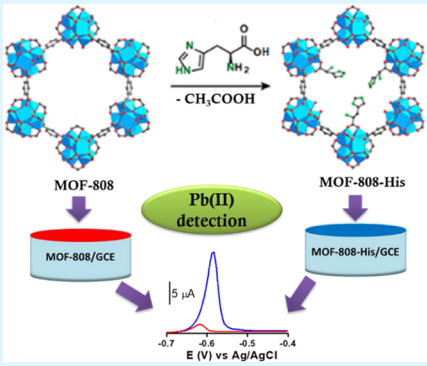

KEYWORDS: *metal−organic framework, lead detection, voltammetry, histidine, glassy carbon electrode*

1. INTRODUCTION

The global apprehension over the discharge of detrimental heavy-metal ions into the environment persists.[1] The bioaccumulation of these toxic heavy metals aggravates the problem and presents a substantial peril to biodiversity and human well-being.[2−4] Lead is among the most toxic heavy metals since it can damage the nervous system (the brain in particular), and liver, even at very low concentrations.[5] Besides general concerns, the occupational hazards associated with plating, mining, tanneries, and oil refining, are among more special problems, particularly in developing countries.[6] As substantiation, the continuous surveillance and traceability of lead remains a perpetual concern for researchers in the domains of analytical chemistry, pollution management, and sensor technologies.[6] The maximum contamination level of lead in drinking water is set at 10 μg L^{-1} (48 nmol L^{-1}) by the World Health Organization (WHO).[7] In order to mitigate the deleterious impact of heavy-metal ions on the environment and human health, the development of detection methodologies with elevated sensitivity and reliability for lead ions holds significant importance. Quantitative determination of lead ions in environmental samples has attracted extensive attention.[8−10]

Many analytical techniques have been proposed for that purpose, such as atomic absorption spectroscopy,[11] atomic emission spectrometry,[12] atomic fluorescence spectrometry,[13] luminescence tests,[14,15] and inductively coupled plasma-mass spectroscopy.[16,17] However, these approaches necessitate costly equipment, labor-intensive protocols, and extensively skilled personnel to attain satisfactory sensitivity. Thus, it is desirable to investigate precise, user-friendly, cost-effective, and highly efficient technologies for the monitoring of Pb^{2+} ions in the environment. Electrochemical methods used for lead determination offer several advantages, including low cost, simplicity, selectivity, and high sensitivity.[6,18] Electrochemical stripping voltammetry is preferred due to its incorporation of an efficient preconcentration process combined with advanced electrochemical measurement techniques for accumulated analytes.[19]

Received: October 24, 2023
Revised: December 15, 2023
Accepted: December 19, 2023
Published: January 3, 2024

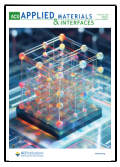

https://doi.org/10.1021/acsami.3c15931
ACS Appl. Mater. Interfaces 2024, 16, 2509−2521

Nevertheless, serving as the fundamental component of electrochemical sensors, the majority of electrode materials encounter numerous constraints, including restricted surface areas (attributable to heightened sensitivity and dynamic range), lack of structural tunability, and limited possibility to modify the surface where the electron transfer process occurs. Consequently, considerable endeavors have been devoted to the advancement of materials exhibiting tailored chemical and physical characteristics, with the aim of enhancing their electrochemical performance. Many materials have been used as electrode modifiers for the detection of heavy-metal ions in water, including organoclays,[6,20−23] carbon nanotubes,[24] and metal−organic frameworks (MOFs).[25−28]

The rise of MOFs has attracted the attention of electrochemists as a promise for better electrode materials. The micro/mesoporous metal−organic framework materials (MOFs, also known as porous coordination polymers, PCPs) could potentially serve as a part of composite electrode materials, ensuring increased surface area with tunable nature/functionalization and pore size, accelerate mass transport, nature, and accelerate electron transfer.[29,30] These attributes make MOFs highly appealing materials for a wide range of applications, including gas/energy storage, adsorption, separation, sensing, drug delivery, and catalysis, which also could mean interesting synergism with their possible use as electrode materials.[31−35] However, most MOFs have poor electronic conductivity and relatively low stability (particularly hydrolytic one).[36,37] Such a disadvantage could hamper the efficiency of MOFs for the determination of lead. MOFs composed of zirconium as the metal ion are regarded as a promising choice, due to the good cation/anion matching in hard and soft acids and bases concept (HSAB) terms.[27] Although they have interesting properties, the adsorption of heavy metals by MOFs, at least by the most typical carboxylate ones, is typically low (particularly from a selectivity and sensitivity point of view), also due to poor HSAB match. One of the still addressable technological problems of MOFs as electrode materials is their limited processability, while the as-synthesized crystalline particles are typically micron-sized, thereby possessing limited adhesion affinity to the electrode surface.[39] A prevalent strategy to surmount these limitations is the integration into MOFs of a matrix or a functional support to improve electrical conductivity and stability.[40,41] An illustrative example involves the utilization of an iron(II) phthalocyanine-derived nanocomposite integrated with Zn-based MOF. This amalgamation demonstrated efficacy in facilitating the electrochemical assessment of trichloroacetic acid.[42]

Another approach is to functionalize MOFs with groups that have a good affinity toward heavy-metal ions. Zr-MOFs functionalized with amino groups (UiO-66-NH_2) are particularly interesting for electrochemical sensing applications, as the abundance of the amino groups favors the adsorption of heavy-metal ions.[27] Another route is the use of thiols/thiolates for even better binding. For example, UiO-66(Zr)−$OOCCH_2SH$ was prepared via modulated synthesis in the presence of thioacetic acid, for the removal of silver from water.[43]

A nanocomposite comprising the Zr(IV)-based MOF NH_2−UiO-66 and reduced graphene oxide (RGO) has been formulated for the electrochemical identification of ciprofloxacin in an aqueous medium.[44] Zirconium carboxylate MOFs are generally promising in this regard due to the inherent availability of defects, at which functionalized carboxylates could be docked. MOF-808, according to our opinion, is particularly interesting in this regard. MOF-808 is built of $[Zr_6O_4(OH)_4]^{12+}$ inorganic building units (IBUs) connected by 1,3,5-benzenetricarboxylate linkers (BTC) to form a highly porous structure with an **spn** topology with good porosity characteristics and reasonable hydrolytic stability. The coordination of the hexanuclear IBUs, typical for zirconium, is completed by the monofunctional carboxylate anions, usually formates or acetates, and the corresponding idealized formula is $[Zr_6O_4(OH)_4(BTC)_2(HCOO)_6]$ or $[Zr_6O_4(OH)_4(BTC)_2(CH_3COO)_6]$.[45] Formic acid, along with other carboxylic acids, is a ligand that appears to act as a crystal growth rate modulator.[46] These coordinated monocarboxylates can be postsynthetically exchanged by other monocarboxylates bearing functional groups, thereby functionalizing the surface of the pores.[45] An interesting possibility is the functionalization of the pores by amino acids: e.g., an example demonstrated the generalization of the approach by synthesizing 11 amino-acid-functionalized MOF-808 structures in which the carboxylate fragment is coordinated to the cluster, while the amino-containing fragment represents a modifying pendant group in the pores of the MOF.[47] The method of preparation in this case was a standard solvothermal synthesis (Scheme 1a,b) using elevated temperatures (150 °C) and extended reaction durations (3−7 days), utilizing the hazardous solvent N,N-dimethylformamide (DMF).[45,48] Therefore, a cleaner, faster, and gentler approach is desirable for the synthesis of MOF-808, so a green synthesis procedure based on water and acetic acid has been developed, using moderate temperatures (100 °C) and short reaction times (5−24 h).[49,50] While the amino-acid-grafted Zr-MOFs are potentially interesting in the context of electrochemical sensing, there is room for improving their synthesis and affinity toward heavy metals.

Scheme 1. (a) Section of the 3D Structure of MOF-808 (Yellow Spheres Depict the Small Tetrahedral Pores). (b) Schematic Depiction of the Substitution of Coordinated Formate in MOF-808 by Histidinate to Give MOF-808-His[a]

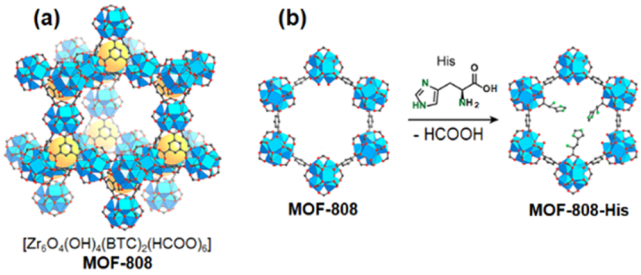

[a]Adapted with permission.[38] Copyright 2018 American Chemical Society.

In this work, we pursued an environmentally sustainable and simple synthesis of MOF-808 in aqueous medium under reflux, followed by postsynthetic acetate modulator exchange with L-histidine (2-amino-3-(1H-imidazol-4-yl)propionic acid = His), which is deemed one of the most promising modifiers for binding heavy metals due to its chelating capabilities via the amino and imidazole functions. The implementation of postsynthetic modulator exchange of acetate vs histidinate seeks to improve the binding of lead ions by forming stable complexes with chelating amino-NH_2- and imidazole-N-donors

https://doi.org/10.1021/acsami.3c15931
ACS Appl. Mater. Interfaces 2024, 16, 2509−2521

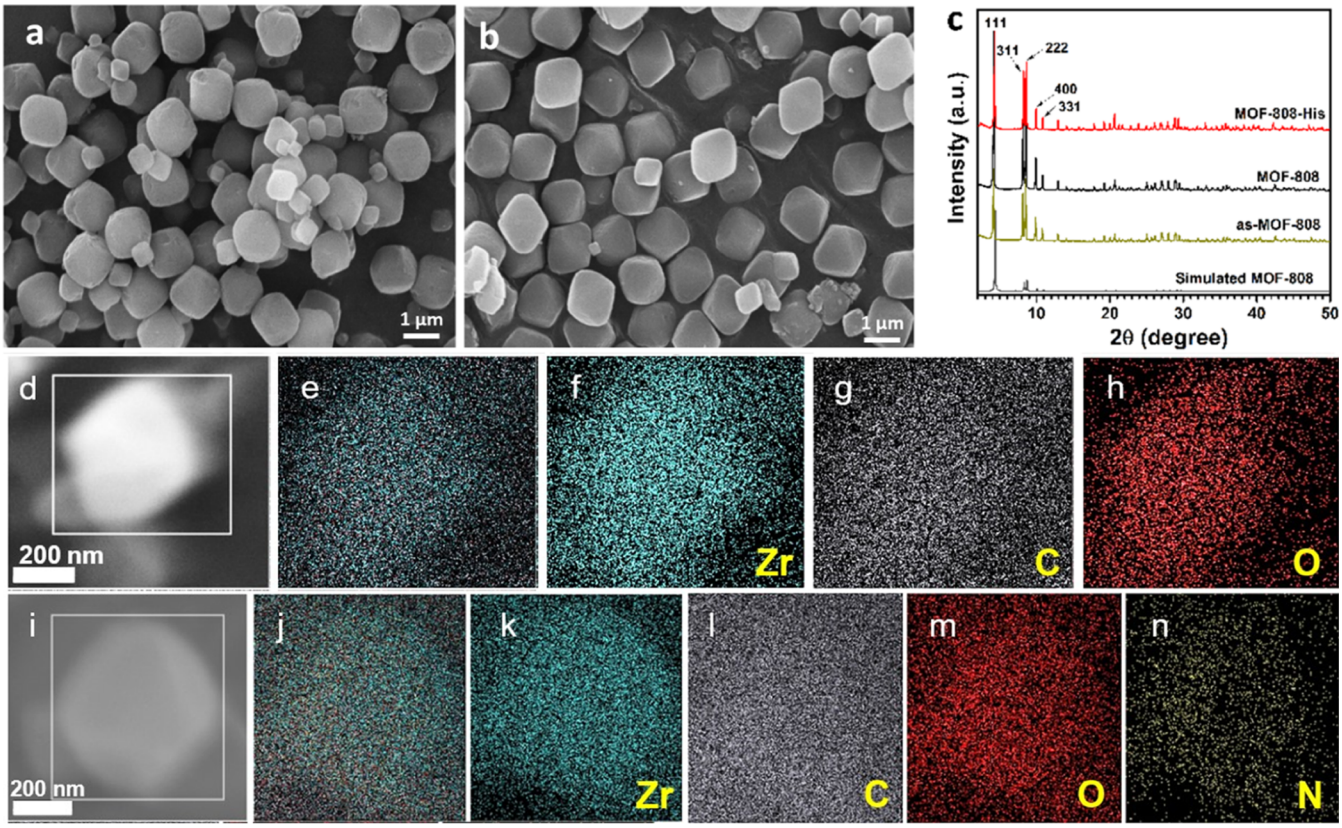

Figure 1. (a, b) SEM images of MOF-808 and MOF-808-His. (c) Powder X-ray diffractograms of simulated MOF-808, as-MOF-808, MOF-808, and MOF-808-His. SEM images and the corresponding EDS-elemental mapping of MOF-808 (d-h) and MOF-808-His (i-n). Superposition of EDS-mappings (e, j).

and Pb^{2+} cations. These complexes can be weakened under acidic conditions, leading to optimal Pb^{2+} ion detection. The MOF-808-His material, acquired through this synthesis, was employed as a modifier for a glassy carbon electrode (GCE) and demonstrated, for the first time, its utility in electrochemical detection of lead ions in aqueous media.

2. EXPERIMENTAL SECTION

2.1. Materials and Chemicals. All reagents employed in the study were commercially obtained and utilized without additional purification. These included zirconyl chloride octahydrate ($ZrOCl_2 \cdot 8H_2O$, purity 99.5%, ChemSolute, Renningen, Germany), benzene-1,3,5-dicarboxylic acid (H_3BTC, purity 98%, BLD Pharmatech, Mehlingen, Germany), deuterium oxide (D_2O, 99.8 atom %D, Karlsruhe, Germany), and sodium nitrate ($NaNO_3$, purity 99%, PanReac AppliChem, Darmstadt, Germany). Acetone (purity 99.5%), ethanol (purity 98%), and histidine (His, purity ≥99%) were obtained from Sigma-Aldrich (Steinhelm, Germany). Lead(II) nitrate ($Pb(NO_3)_2$, purity 99%), potassium hexacyanidoferrate(III) ($K_3[Fe(CN)_6]$, purity ≥99%), and potassium hexacyanidoferrate(II) trihydrate ($K_4[Fe(CN)_6] \cdot 3H_2O$, purity > 98%) were obtained from Merck (Darmstadt, Germany). Hexaammineruthenium(III) chloride ($[Ru(NH_3)_6]Cl_3$, purity 97%), hydrochloric acid (HCl, purity 37%), and sodium hydroxide (NaOH, purity >98%) were obtained from Sigma-Aldrich (Steinhelm, Germany). All solvents were of analytical grade. Ultrapure water was used to prepare all solutions. pH measurements were conducted using a Metrohm 744 pH meter equipped with a glass electrode.

2.2. Synthesis of MOF-808 and Postsynthetic Grafting of Histidine to MOF-808-His. MOF-808 was synthesized under the reflux method according to a published procedure.[49] The as-synthesized material, designated as as-MOF-808, underwent overnight vacuum activation (10^{-3} mbar) at a temperature of 60 °C, resulting in a yield of 875 mg. MOF-808 was histidine-functionalized according to a procedure described in the literature.[51] The sample MOF-808-His was then dried at 60 °C overnight under vacuum (10^{-3} mbar).

2.3. Physicochemical Characterization of MOFs. The crystallographic properties and phase composition of the materials were evaluated via powder X-ray diffraction (PXRD) analysis. This analysis was performed using a Rigaku MiniFlex600 diffractometer equipped with a 600 W Cu−Kα X-ray source (40 kV, 15 mA), operating in reflective mode within the 2θ range of 2−100°. The experimental setup included a Bragg−Brentano goniometer, a graphite monochromator, and a HyPix-400 MF 2D hybrid pixel array detector (HPAD). The measurement was performed at room temperature with 0.01° steps using Cu−Kα radiation (λ = 1.54182 Å). Fourier-transform infrared spectroscopy (FTIR), nitrogen physisorption isotherms, thermogravimetric analysis (TGA), scanning electron microscopy (SEM), and elemental analysis were performed using the instrumentation detailed in ref 43. Spatial distribution analysis of elemental composition was conducted through energy-dispersive spectrometry (EDS) mapping, employing a scanning electron microscope (SEM) ZEISS EVO with energy-dispersive X-ray spectroscopy (Carl Zeiss GeminiSEM 500, Germany). Prior to analysis, all samples were subjected to overnight vacuum drying at 60 °C. ^{1}H nuclear magnetic resonance (NMR) spectra were acquired using an AVANCE III Bruker HD 300 MHz Digital NMR spectrometer. 128 scans were collected with longer than typical d1 relaxation times at 20 s were collected to ensure reliable integrals.

2.4. Digestion of the MOF for the ^{1}H NMR Spectroscopy Analysis. The sample preparation of MOFs prior to the liquid ^{1}H NMR analysis was carried out according to a protocol described in the literature.[51] The MOFs samples (about 15 mg) were ultrasonically dissolved in a $NaOH/D_2O$ solution for 24 h before collecting their ^{1}H NMR spectra. This procedure allows only the organic part of the MOFs to be dissolved. The residual formed Zr-oxide hydroxide was removed by filtration.

https://doi.org/10.1021/acsami.3c15931
ACS Appl. Mater. Interfaces 2024, 16, 2509−2521

2.5. Preparation of Working Electrodes. The sensors were elaborated by the "drop coating" method on a GCE (Ø = 3 mm). The latter was first polished with a 0.05 μm alumina paste and then rinsed with pure water. The prepared MOF-808-His was dispersed in ultrapure water by ultrasonication to reach a concentration of 2 mg mL^{-1}. Then, 2 μL of the suspension was deposited on the surface of the GCE and oven-dried at 40 °C for 10 min to form a modified electrode, designated as MOF-808-His/GCE. The MOF-808-modified GCE, designated as MOF-808/GCE and used for comparison, was also prepared using the same procedure.

2.6. Electrochemical Studies. Voltammetric measurements were conducted at ambient temperature using a Metrohm 797 VA Computrace, employing a standard three-electrode cell configuration. The working electrodes consisted of either bare or modified GCEs, while a silver/silver chloride electrode (Ag/AgCl) served as the reference electrode, and a platinum electrode (Pt) functioned as the auxiliary electrode. Cyclic voltammograms of $[Fe(CN)_6]^{3-}$ and $[Ru(NH_3)_6]^{3+}$ ions were recorded within the potential range of −0.3 to 0.6 V and −0.55 to 0 V, respectively, in an aqueous solution of 0.1 mol L^{-1} $NaNO_3$. The scan rate used was 20 mV s^{-1} (unless otherwise specified), and no stirring of the supporting electrolyte was performed. Electrochemical impedance spectroscopy (EIS) measurements were carried out using a Gamry instrument Interface1000TM controlled by Gamry framework software. EIS was conducted over a frequency range of 0.1 Hz to 10 kHz, with a potential amplitude of 10 mV and a fixed potential of 0.2 V. The electrolyte employed for EIS measurements was a 0.1 mol L^{-1} aqueous $NaNO_3$ solution containing 0.5 mmol L^{-1} $[Fe(CN)_6]^{3-}/[Fe(CN)_6]^{4-}$. The results obtained were processed using the Echem analyst software. The electroanalysis of Pb^{2+} ions was performed using square wave voltammetry (SWV). The electrochemical detection protocol comprises two sequential stages: an open-circuit preconcentration (accumulation) step of the analyte, succeeded by voltammetric detection in a distinct medium, specifically a hydrochloric acid solution. The initial step involved immersing the working electrode in a beaker containing 20 mL of Pb^{2+} solution with a specified concentration, maintained under gentle agitation. Following a predetermined accumulation period, the electrode was promptly extracted, rinsed with ultrapure water, and transferred to the electrochemical cell housing the detection solution. All experiments were carried out in triplicate and the data points are an average of three repeated experiments.

3. RESULTS AND DISCUSSION

3.1. Physicochemical Characterization of MOFs. *3.1.1. SEM and PXRD Analyses.* SEM micrographs of MOF-808 and MOF-808-His are shown in Figure 1a,b. The images obtained show the octahedral morphology of all materials, with no significant change in the microcrystal shape of MOF-808 after the modification with histidine. Most microcrystals have a size of around 1 μm. PXRD characterizations were performed to verify the crystalline MOF-808 phase of the materials by positive matching with the simulated patterns (Figure 1c). The matching PXRD pattern proved the MOF-808 formation and exhibited the high crystallinity of the synthesized structures, thereby verifying the phase purity and unchanged crystalline structure following the incorporation of amino acids. Diffraction peaks at 2θ = 4.28, 8.30, 8.69, 9.92, and 10.93° were related to the (111), (311), (222), (400), and (331) planes, respectively. The crystallinity index (CI) of the materials was estimated by analyzing the integrated intensity areas (crystalline peak areas) of the characteristic X-ray diffraction peaks after baseline correction,[52] according to the equation: $CI = \frac{\text{area of crystalline peaks}}{\text{area of all peaks}} \times 100$. MOF-808 and MOF-808-His showed a good crystallinity index with values of 83 and 82%, respectively. The energy-dispersive X-ray spectroscopy (EDS) element mappings were conducted on a single particle depicted in Figure 1d−n and on many particles (Figure S1a−k in the Supporting Information) to examine the element compositions of MOF-808 and MOF-808-His. The spatial distribution of Zr, C, O, and N superimposes satisfactorily for MOF-808 and MOF-808-His.

3.1.2. ^{1}H NMR and Elemental Analysis. The amount of His moieties in MOF-808-His was estimated by ^{1}H NMR spectroscopy of digested samples. The ^{1}H NMR spectra of pristine MOF-808, His, and MOF-808-His after digestion of the samples in $NaOH/D_2O$ solution for 24 h are shown in Figure 2. The chemical shift at 8.3 ppm in all spectra

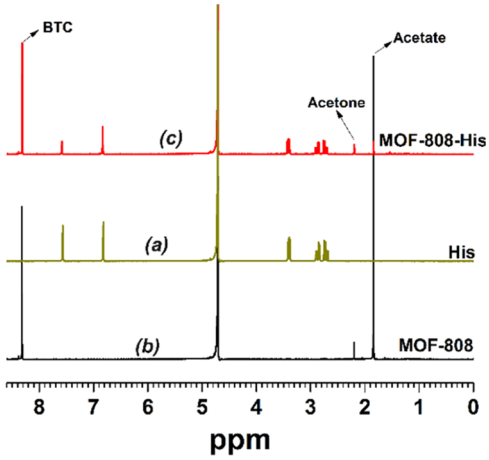

Figure 2. ^{1}H NMR spectra of (a) histidine, and digestion NMR spectra of (b) MOF-808 and (c) MOF-808-His in $NaOH/D_2O$ (the signal at 4.7 ppm is from residual HDO/D_2O).

corresponds to the 3 protons of the aromatic ring of BTC^{3-}. The chemical shifts at 1.85 and 2.2 ppm stem from the protons of the acetate and acetone (due to washing step) groups, respectively. The acetate group content in the MOF-808 framework was calculated from the ratio of the integrated peak areas of acetate and BTC (Figures S2 and S3 in the Supporting Information). The Ac/BTC molar ratio was determined to be 1.9:1, indicating that approximately 3.8 acetate groups are bound to each $Zr_6O_4(OH)_4$ SBU in the formula unit of MOF-808 (see details of the calculations in the Supporting Information). This is less than the 3:1 ratio expected for the ideal formula $[Zr_6O_4(OH)_4(BTC)_2(Ac)_6]$.[45,46] Yet, this ratio of Ac/BTC of ≈2:1 was also matched by CH analysis (cf. Table S1 in the Supporting Information). The missing 2.2 acetate groups in the synthesized MOF-808 are apparently replaced by $4.4H_2O$ ligands bound to the Zr sites and $2.2OH^-$ being hydrogen-bonded to the μ_3−OH groups. Such a replacement was structurally authenticated in a single-crystal structure of the related MOF UiO-66.[53]

The formula unit of the synthesized MOF-808 then corresponds to $[Zr_6O_4(OH)_4(BTC)_2(Ac)_{3.8}(OH)_{2.2}(H_2O)_{4.4}]$. The integral intensity of the acetate group of MOF-808 decreased significantly in the case of MOF-808-His, demonstrating the successful substitution of acetate ligands by L-histidine. The L-histidine proton signals were observed in the ^{1}H NMR spectra of MOF-808-His (Figure S4). The acetate and His contents on the MOF-808 network were calculated based on the ratios of the integrated peak areas of acetate/BTC and His/BTC. The acetate and His contents on the MOF-808 network were calculated based on the ratios of the integrated peak areas of acetate/BTC and His/BTC. For MOF-808-His,

https://doi.org/10.1021/acsami.3c15931
ACS Appl. Mater. Interfaces 2024, 16, 2509−2521

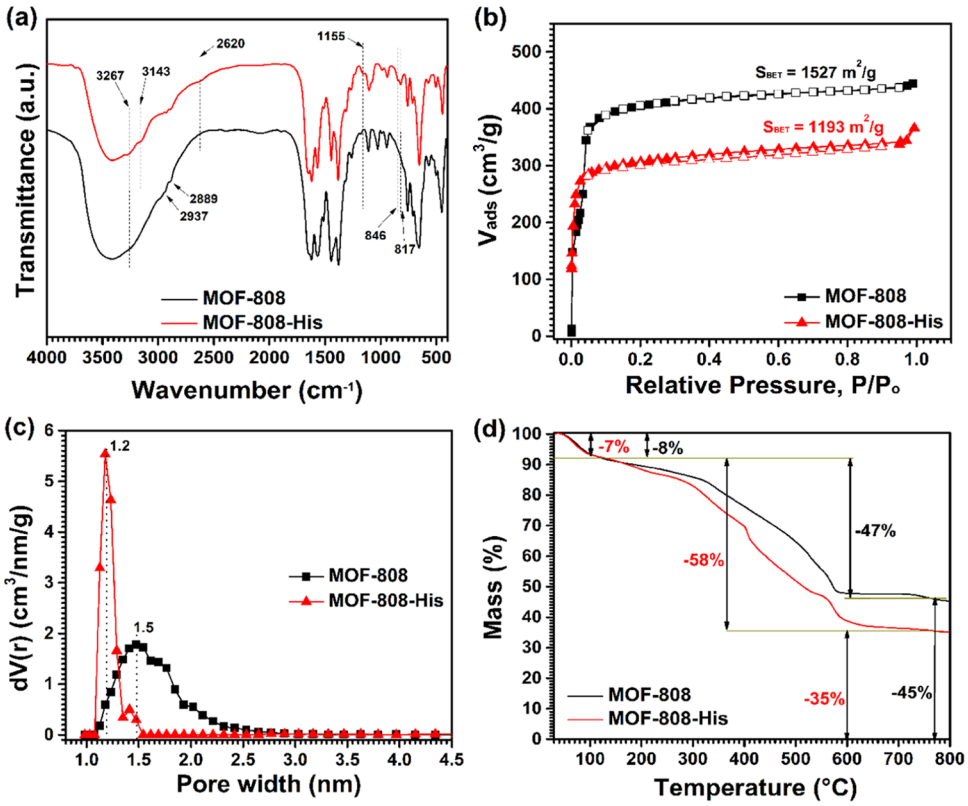

Figure 3. (a) FT-IR spectra, (b) N_2 adsorption−desorption isotherms measured at 77 K, where filled symbols represent adsorption and empty symbols represent desorption, (c) pore size distribution plot, and (d) TGA curves of MOF-808 (black line), and MOF-808-His (red line).

Ac/BTC and His/BTC molar ratios of 0.14:1 and 1.8:1 were obtained, respectively, indicating that about 3.6 His groups coordinate to each $Zr_6O_4(OH)_4$ SBU in the formula unit of MOF-808-His and only about 0.28 acetate groups remain. This then gives a composition for MOF-808-His of $[Zr_6O_4(OH)_4(BTC)_2(Ac)_{0.3}(OH)_{2.1}(His)_{3.6}(H_2O)_{4.2}]$ which is also matched by CHN analysis (cf. Table S1 in the Supporting Information). Noteworthy, the derived formulas for synthesized MOF-808 and MOF-808-His are approximate since they assume the ideal BTC content of 2 and do not account for possible BTC linker defects.

3.1.3. FT-IR, BET, and TG Analyses. FT-infrared spectroscopy was employed to follow the incorporation of L-histidine (Figure 3a). The peak at ∼653 cm^{-1} corresponds to the vibrational mode of Zr−O bonds,[54] while the characteristic peaks at 1375, 1450, and 1577 cm^{-1} are attributed to the stretching vibrations of carboxylate groups of the BTC ligands. The absorption bands at 763 cm^{-1} belong to out-of-plane vibrations of the BTC ring. In the spectrum of MOF-808-His, the emerging peak of C−N stretching of the amino group was observed at 1155 cm^{-1}, and a set of twin peaks of $-NH_2$ stretching of the amino group at 3267 and 3143 cm^{-1}, which indicate that the MOF-808 was functionalized with histidine. Figure 3b,c displays the N_2-sorption isotherms and the NLDFT pore size distribution (Calculation model: N_2 at 77 K on carbon) plots for MOF-808, and MOF-808-His. Both display type I nitrogen isotherms, which are typical of microporous materials.[49,52] MOF-808 demonstrates a Brunauer−Emmett−Teller (BET) surface area of 1527 m^2 g^{-1}, a pore volume of 0.69 cm^3 g^{-1} and an average pore size of 1.5 nm. In comparison, MOF-808-His has smaller BET surface area (1193 m^2 g^{-1}), pore volume (0.47 cm^3 g^{-1}), and average pore size (1.2 nm). The changes reflect the successful partial exchange of the acetate by histidinate in the framework. It should be noted that the cavity size in two samples is still large enough for efficient mass transfer of the solvated ions in the pores (the adsorption kinetics in aqueous solution depends on the size of the hydrated ions which are 0.4 nm for Pb^{2+} and 0.32 nm for NO_3^-;[55] with 0.12 and 0.18 nm respective ionic radii).[53] The value of the specific surface area, determined in this investigation for MOF-808 (1527 m^2 g^{-1}) agrees with other BET surface area reports for MOF-808 from acetic acid modulated synthesis in water (1210 and 1540 m^2 g^{-1}).[50,54] However, this value is lower than the early reported BET surface area for MOF-808 (2060 m^2 g^{-1}) which was synthesized under formic acid modulation,[45] which resulted in a material featuring coordinated formate anions decorating the inner pores of the framework. The material obtained in this work has acetate coordinated in the pores. The lower surface area and porosity is, therefore, due to the higher steric occupation of acetate compared to formate in the pores of MOF-808. The thermal stability and chemical compositions of our materials can be assessed by thermogravimetric analysis (TGA) (Figure 3d). Prior to TGA testing, the samples were activated by solvent exchange and subsequently subjected to vacuum evacuation at 60 °C overnight. TGA curves of pristine MOF-808 and histidine-grafted MOF-808 materials under synthetic air conditions are presented in Figure S5 (Supporting Information). The first step (up to 100 °C) observed on the TGA curve is ascribed to the loss of Zr-coordinated water (aqua ligands). Both MOF-808 and MOF-808-His have a very similar crystal water content. The second step started from 105 to 800 °C and can be attributed to the loss of the coordinated water (aqua ligands), the acetate CH_3COO^- modulator, and

https://doi.org/10.1021/acsami.3c15931
ACS Appl. Mater. Interfaces 2024, 16, 2509−2521

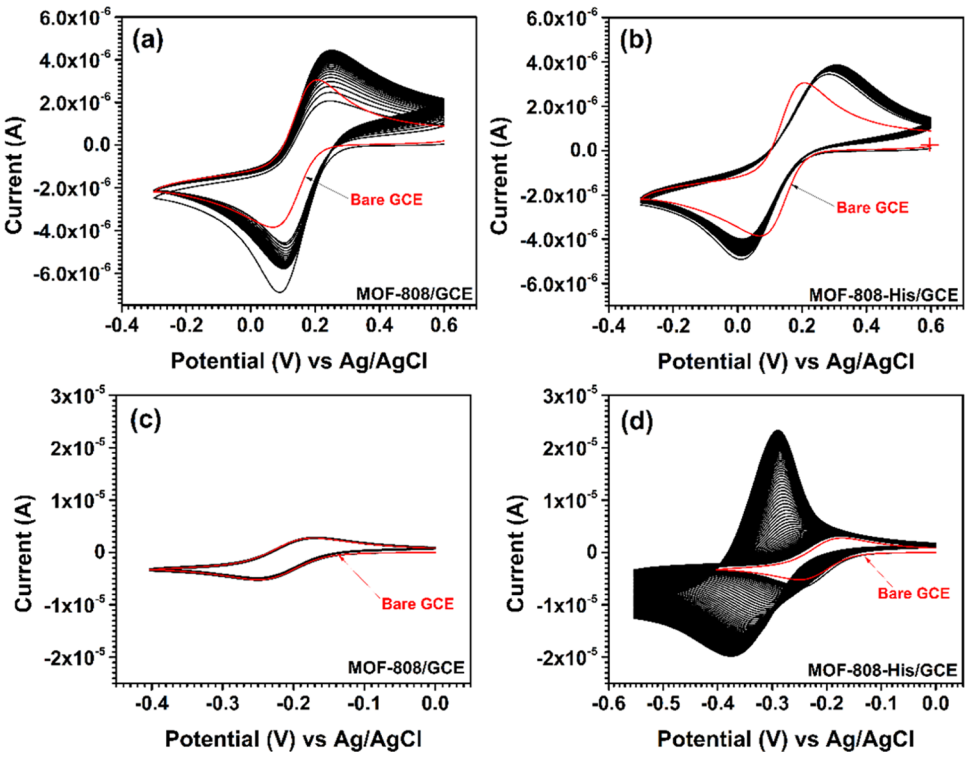

Figure 4. Multicyclic voltammograms of 0.5 mmol L^{-1} $[Fe(CN)_6]^{3-}$ in 0.1 mol L^{-1} $NaNO_3$ (pH 6.5) on (a) MOF-808/GCE and (b) MOF-808-His/GCE at a scan rate of 50 mV s^{-1}. Multicyclic voltammograms of 0.5 mmol L^{-1} $[Ru(NH_3)_6]^{3+}$ in 0.1 mol L^{-1} $NaNO_3$ (pH 6.5) on (c) MOF-808/GCE and (d) MOF-808-His/GCE at scan rate of 50 mV s^{-1}.

the organic linker (BTC) (cf. Table S1 in the Supporting Information). The mass loss during this step was lower for MOF-808 (47 wt %) than for MOF-808-His (58 wt %), suggesting that some of the acetates were replaced by histidine molecules during the grafting process. The plateau from about 800 °C on can be fully regarded as the residue ZrO_2. The residual ZrO_2 content at 800 °C (35 wt %) in MOF-808-His is lower than the residual content in MOF-808 (45 wt %). The findings derived from elemental microanalysis, comparison of infrared (IR) spectra, thermogravimetric (TG) analysis, ^1H nuclear magnetic resonance (NMR) spectroscopy, and N_2 adsorption−desorption isotherm analysis collectively indicate the successful substitution of acetate groups by histidine molecules within MOF-808.

3.2. Electrochemical Characterization of Modified GCE and Assessment of Electrochemical Sensing Capabilities for Positive and Negative Ions. Cyclic voltammetry (CV) and electrochemical impedance spectroscopy (EIS) are useful techniques to study the electrochemical characteristics of the modified electrode.

3.2.1. Cyclic Voltammetry (CV). CV was employed to examine the electrochemical behavior of the modified electrodes toward $[Fe(CN)_6]^{3-}$ and $[Ru(NH_3)_6]^{3+}$ electroactive probes. CV experiments were conducted in 0.1 mol L^{-1} $NaNO_3$ at two different pH values: pH 6.5 and pH 3 (obtained by diluting a 0.1 mol L^{-1} HCl solution). The bare GCE, MOF-808/GCE, and MOF-808-His/GCE were utilized for the CV measurements at a scan rate of 50 mV s^{-1}. These experiments aimed to evaluate the ion exchange properties of the materials (MOF-808 and MOF-808-His) and to confirm the presence of amino acid moieties in the modified material. The analysis of $[Fe(CN)_6]^{3-}$ was performed in a potential range of −0.3 to 0.6 V in 0.1 mol L^{-1} $NaNO_3$ at pH 6.5, and the obtained results are depicted in Figure 4a,b. The bare GCE gave a reversible system (I_{pa}/I_{pc} = 1). Compared to bare GCE, MOF-808/GCE showed larger peak currents in the first cycle, especially in the cathodic direction (I_{pa} = 3.6 μA, I_{pc} = 6.8 μA) and slight accumulation. This accumulation occurs with a shift of the peak potentials from 0.012 V to cathodic values to give peak currents of 4.8 μA (anodic direction), and 5.8 μA (cathodic direction) at the 35th scan.

The adsorption of the redox species is allowed by the pore size (1.5 nm) and takes place due to the good surface area (1527 m^2 g^{-1}) and the possibility of terminal ligand exchange (acetate in this case) or defect filling. In contrast, a slight accumulation, and peak current of the 35th scan of 3.95 μA (anodic direction), and 3.6 μA (cathodic direction) were obtained with MOF-808-His/GCE (Figure 4b). This accumulation occurs as a result of electrostatic attraction between the negatively charged redox system $[Fe(CN)_6]^{3-}$ and the amino group of histidine, which carries a positive charge; this process should strongly depend on the pH and increases with the protonation of the amino group of the histidine (at least until pH levels low enough to fully protonate the amino group of the histidine).

The low peak current values compared to those obtained on MOF-808/GCE are reflected in the decrease of its specific surface area (1193 m^2 g^{-1}) and pore diameter (1.2 nm) and a low efficiency of histidine as a ligating pendant group under standard conditions. However, in an acidic environment pH 3 (obtained by dilution from a 0.1 mol L^{-1} HCl solution), the peak currents increased significantly for all electrodes (Figure S6, in the Supporting Information). On MOF-808-His/GCE (Figure S6b in the Supporting Information), a progressive accumulation of $[Fe(CN)_6]^{3-}$ species was noted, which stabilized after about 50 scans, with peak current values (I_{pa}

https://doi.org/10.1021/acsami.3c15931
ACS Appl. Mater. Interfaces 2024, 16, 2509−2521

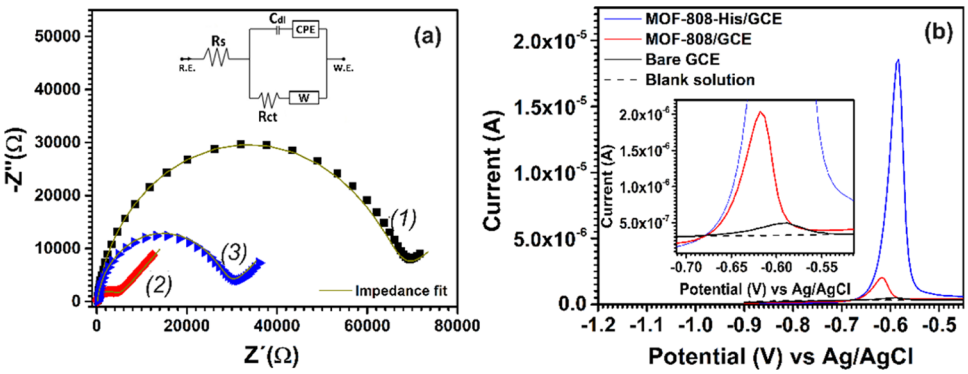

Figure 5. (a) Nyquist diagrams of electrochemical impedance spectra of 0.5 mmol L^{-1} $Fe(CN)_6^{3-/4-}$ in 0.1 mol L^{-1} $NaNO_3$ (pH 6.5) at (1) bare GCE, (2) MOF-808/GCE, and (3) MOF-808-His/GCE. Inset: Equivalent circuit model. Experiments were performed in triplicate (n = 3). (b) SWASV of 10 μmol L^{-1} of Pb^{2+} in 0.1 mol L^{-1} HCl on MOF-808-His/GCE, MOF-808/GCE, and bare GCE. The dotted curve corresponds to the blank solution. Deposition potential, −1.2 V; deposition time, 30 s.

= 21.1 μA, I_{pc} = 43.5 μA), higher than those obtained on bare GCE (I_{pa} = 5.2 μA, I_{pc} = 5.2 μA) and on MOF-808/GCE (I_{pa} = 10 μA, I_{pc} = 17 μA) (Figure S6a in the Supporting Information). This accumulation arises from the electrostatic attraction between the negatively charged $[Fe(CN)_6]^{3-}$ redox probe species and the highly protonated amino groups that are present on the surface of MOF-808 following the grafting of histidine.

Moreover, under neutral conditions, the peak-to-peak separations (ΔE) observed at MOF-808-His/GCE and MOF-808/GCE were measured to be 0.291 and 0.159 V (with a value of 0.149 V from the second to the 35th scan), respectively. This disparity can be ascribed to the enhanced electron transfer kinetics and larger electroactive surface area exhibited by MOF-808/GCE when compared to MOF-808-His/GCE. Under nearly neutral conditions (pH 6.5), the diffusion of cations within MOF-808-His surpasses that of pristine MOF-808. This is attributed to the electrostatic attraction between the positively charged MOF-808-His, which is protonated at this pH, and $[Fe(CN)_6]^{3-}$ ions.

Similarly, the analysis of $[Ru(NH_3)_6]^{3+}$ species was performed in the potential range of −0.55 to 0.0 V in 0.1 mol L^{-1} $NaNO_3$ at pH 6.5 and the results are shown in Figure 4c,d. The response of the probe on bare GCE was also reversible ($I_{pa}/I_{pc} \approx 1$). By modifying the bare GCE with MOF-808 (Figure 4c), peak currents comparable to those obtained on bare GCE (I_{pa} = 4.4 μA, I_{pc} = 5.2 μA) were obtained. A substantial disparity is evident when comparing the findings obtained from MOF-808/GCE and MOF-808-His/GCE. The multicyclic voltammograms recorded on MOF-808/GCE with accumulated $[Ru(NH_3)_6]^{3+}$ (Figure 4c) show a couple of oxidation and reduction peaks centered at ∼0.214 V. On the other hand, for MOF-808-His/GCE (Figure 4d), this couple also appears (at ∼0.214 V) demonstrating a slight accumulation (I_{pa} = 4.4 μA, I_{pc} = 6.5 μA) before and during the first scan. During further scans, a notable potential shift of the redox peaks toward more negative values (redox couples centered at ∼0.318 V) was observed, as well as a significant accumulation, leading to higher peak currents after 75 scans (I_{pa} = 14.2 μA, I_{pc} = 19.7 μA). The observed behavior related to the $[Ru(NH_3)_6]^{3+}$ species for MOF-808-His material is not common. One could suggest that the signals centered at ∼0.214 V are due to the interaction between the $[Ru(NH_3)_6]^{3+}$ species and the MOF-808-His material. Further, the signals centered at ∼0.318 V are due to "free" $[Ru(NH_3)_6]^{3+}$ species in the solution that have been exchanged for cations in the electrolyte prior to their electrochemical reduction. Under acidic conditions (pH 3), the peak currents were almost the same on all electrodes (Figure S6 in the Supporting Information): bare GCE (I_{pa} = 4.6 μA, I_{pc} = 5.4 μA), MOF-808/GCE (I_{pa} = 4.4 μA, I_{pc} = 5.3 μA) and MOF-808-His/GCE (I_{pa} = 4.4 μA, I_{pc} = 5.5 μA). On MOF-808/GCE (Figure S7a in the Supporting Information), this low current can be explained by the fixation of the negative probe $[Fe(CN)_6]^{3-}$ and a positive surface charge of MOF-808 could be hypothesized.

The behavior on MOF-808-His/GCE (Figure S7b in the Supporting Information) is consistent with the phenomenon of electrostatic repulsion between the $[Ru(NH_3)_6]^{3+}$ species and the positively charged MOF-808-His surface due to the presence of the (partially protonated) His molecule. This demonstrates that the charge selectivity of MOF-808-His remained effective on the GCE, allowing rapid transport/accumulation of anions regardless of the pH of the test medium (neutral and acidic) and cations in neutral media, while preventing cation uptake in acidic media. This result is promising for the exploitation of MOF-808 and MOF-808-His as electrode material. CV experiments were performed at various scan rates (Figure S8) and the electroactive surface area of both the unmodified and modified electrodes was determined by calculating the slope of the current plotted against the square root of the scan rate, in accordance with Randles−Ševčik equation:[56] $I_p = (2.69 \times 10^5)An^{3/2}D^{1/2}Cv^{1/2}$, where I_p is the peak current, A the electrode electroactive area (cm^2), n the number of electrons transferred (n = 1), D the diffusion coefficient of $[Fe(CN)_6]^{3-/4-}$ in 0.1 M $NaNO_3$ solution ($D = 7.7 \times 10^{-6}$ cm^2 s^{-1}), C the concentration of $[Fe(CN)_6]^{3-}$ (5×10^{-7} mol cm^{-3}) and v the potential scan rate (V s^{-1}). From the slope of linear plots of I_{pc} vs $v^{1/2}$ (Figure S8b, S8d, and S8f), the electroactive surface areas of bare GCE, MOF-808/GCE, and MOF-808-His/GCE were determined to be 0.053, 0.103, and 0.096 cm^2, respectively. The electroactive surface area of MOF-808/GCE is approximately 1.1-fold higher than that of MOF-808His/GCE and 1.9-fold higher than the bare GCE one. The better electroactive surface area with MOF-808/GCE compared to MOF-808-His/GCE is due to its higher specific surface area and pore diameter, evidence of the presence of a greater number of electrochemically active sites. The presence of (partially protonated) His molecules inside the pores (MOF-808-His) contributes to the number of active sites affine to the $[Fe(CN)_6]^{3-/4-}$ species.

https://doi.org/10.1021/acsami.3c15931
ACS Appl. Mater. Interfaces 2024, 16, 2509−2521

3.2.2. Electrochemical Impedance Spectroscopy. EIS, with Nyquist plots, was employed to elucidate the heterogeneous electron transfer characteristics at the interface between the electrode and the solution. The Nyquist plots exhibited distinct semicircular and linear regions, corresponding to electron transfer-limited and diffusion-limited processes, respectively. The plots were fitted using a variant of the model corresponding to a constant phase element (CPE) with diffusion circuit (Figure 5a, solid line). The resistance of charge transfer (R_{ct}) values obtained with MOF-808/GCE (4196 Ω) was smaller than those obtained on MOF-808-His/GCE (28,080 Ω) and on bare GCE (65,450 Ω), thereby meaning an increased electron transfer rate at the modified electrodes. The R_{ct} values obtained with MOF-808/GCE are lower due to its high electroactive (0.103 cm^2) and BET (1527 $m^2\ g^{-1}$) surface areas. The His molecule has two basic centers, which in the conjugate acid form could express Coulombic interactions with the negative redox probe $[Fe(CN)_6]^{3-/4-}$, resulting in higher electron transfer of MOF-808-His/GCE than bare GCE.

The findings from EIS align with those obtained in CV. Furthermore, the double-layer capacitance (C_{dl}) of bare GCE and modified GCEs was also obtained, and the corresponding circuit elements were compiled and presented in Table 1. The higher C_{dl} value on MOF-808/GCE (19,560 × 10^9 F) than on MOF-808His/GCE (26.02 × 10^6 F) shows that MOF-808-modified electrodes could be a promising material for developing a capacitive sensor.

Table 1. Summary of the Computed Circuit Components for EIS Measurements

electrode	R_s (Ω)	W (μF)	R_{ct} (Ω)	C_{dl} (10^9 F)	k^0 (10^{-6} cm s^{-1})
bare GCE	189.6	108.2	65,450	338.1	1.15
MOF-808/GCE	176.6	91.48	4196	19,560	18
MOF-808-His/GCE	191.3	121.6	28,080	0.026	2.69

For all electrodes, the standard heterogeneous rate constant was also calculated in accordance with the equation[57] $R_{ct} = \frac{RT}{n^2F^2CAk^0}$, where k^0 represents the standard heterogeneous electron transfer rate constant (cm s^{-1}), n is the number of electrons transferred, R stands for the universal gas constant (8.314 J K^{-1} mol^{-1}), T is the temperature (298.15 K), F is the Faraday constant (96,485 C·mol^{-1}), R_{ct} is the electron transfer resistance (Ω), A is the electrode surface area (cm^2), and C is the concentration of the $[Fe(CN)_6]^{3-/4-}$ solution (5 × 10^{-7} mol cm^{-3}). A system characterized by a low k^0 value exhibits a longer time scale to reach equilibrium compared to a system with a high k^0 value, which achieves equilibrium in a shorter time scale. Thus, the k^0 values (Table 1) show that MOF-808/GCE (1.80 × 10^{-5} cm s^{-1}) has a faster electron transfer than MOF-808-His/GCE (2.69 × 10^{-6} cm s^{-1}) as well as the bare GCE (1.15 × 10^{-6} cm s^{-1}). The findings obtained from CV and EIS are in good correlation when experiments are conducted under identical pH conditions (pH 6.5) (refer to Figure 4a,b for CV and Figure 5a for EIS).

The elevated peak currents observed for $[Fe(CN)_6]^{3-}$ ions on MOF-808/GCE correspond to a lower obtained R_{ct} value. Conversely, the diminished peak currents observed on MOF-808His/GCE align with a significantly higher R_{ct} value obtained with MOF-808/GCE.

The elevated peak currents obtained for $[Fe(CN)_6]^{3-}$ ions on MOF-808/GCE correspond to a lower obtained R_{ct} value. Conversely, the diminished peak currents observed on MOF-808His/GCE align with a significantly higher R_{ct} value obtained with MOF-808/GCE.

3.3. Application of the MOF-808-His to the Electrochemical Detection of Pb^{2+}. *3.3.1. Initial Voltammetric Investigations Conducted on Electrodes Modified with Binder-Free MOF-808.* The ability of the previously characterized materials to accumulate lead ions was assessed by square wave anodic stripping voltammetry (SWASV) and the results are presented in Figure 5b. Low peak currents were observed on bare GCE (0.23 μA) and MOF-808/GCE (1.67 μA). The substantial increase in peak current, reaching a factor of 7.3, observed on MOF-808/GCE can be attributed to the notable specific surface area of MOF-808, which facilitates the accumulation of a greater quantity of Pb^{2+} ions from the solution. This high current (1.67 μA) is also reflected by the fact that MOF-808/GCE has a higher electrochemically active surface area than bare GCE. MOF-808-His/GCE shows a better peak current of Pb^{2+} (18.45 μA), with anodic current peak intensities for Pb^{2+} by 11.05 and 80.22 times higher than the ones for MOF-808/GCE and bare GCE, respectively.

The electrochemical lead ion detection process comprises two successive stages: (i) an open-circuit preconcentration or accumulation phase, where lead ions (pH 6) interact with the MOF-808 and MOF-808-His materials. MOF-808-His binds better to the analyte due to its amino-NH_2- and imidazole-N-donors. (ii) The second phase involves voltammetric detection in a separate medium (0.1 mol L^{-1} HCl), where previously accumulated ions are released from the material by ion exchange with protons. This preconcentration is more difficult to achieve with nonfunctionalized MOF-808, resulting in reduced peak currents. Acid solutions are commonly used in electroanalysis due to their ability to weaken complexes formed by cationic species with amine ligands, as shown by previous studies.[58] This preconcentration ability allows the better determination of lead ions by the MOF-808-His/GCE sensor. The results of the electrochemical characterizations using the redox probes showed that the sensitivity of MOF-808 is better for negative charges via coordination bound, explaining the low peak current of Pb^{2+} ions observed on MOF-808/GCE compared to MOF-808-His/GCE. However, Pb^{2+} is mainly present in the form of lead monohydroxide complex $Pb(OH)^+$, which could be efficiently bound by histidine, ensuring better performance of the MOF-808-His material.

3.3.2. Experimental Optimization of the Electrochemical Detection of Lead. In order to obtain the best detection efficiency on MOF-808-His film-modified GCE, a range of relevant parameters for the detection of Pb^{2+} were optimized: amount of MOF-808-His on the electrode, pH of the detection medium, quantity of material in the film, accumulation time, pH of accumulating medium, deposition potential and deposition time. The binding capacity of the MOF-808-His film for Pb^{2+} depends on the amount of the latter present in the dispersion used to modify the electrode surface. Figure 6a demonstrates that the intensity of the anodic peak progressively increases with the amount of material until it reaches a maximum value at 6 μg of MOF-808-His. Above 6 μg, a slight decrease in peak current intensity is observed, indicating that the film has become excessively thick and hinders the efficient detection of the analyte. 6 μg is therefore considered the optimum amount for further investigation.

https://doi.org/10.1021/acsami.3c15931
ACS Appl. Mater. Interfaces 2024, 16, 2509−2521

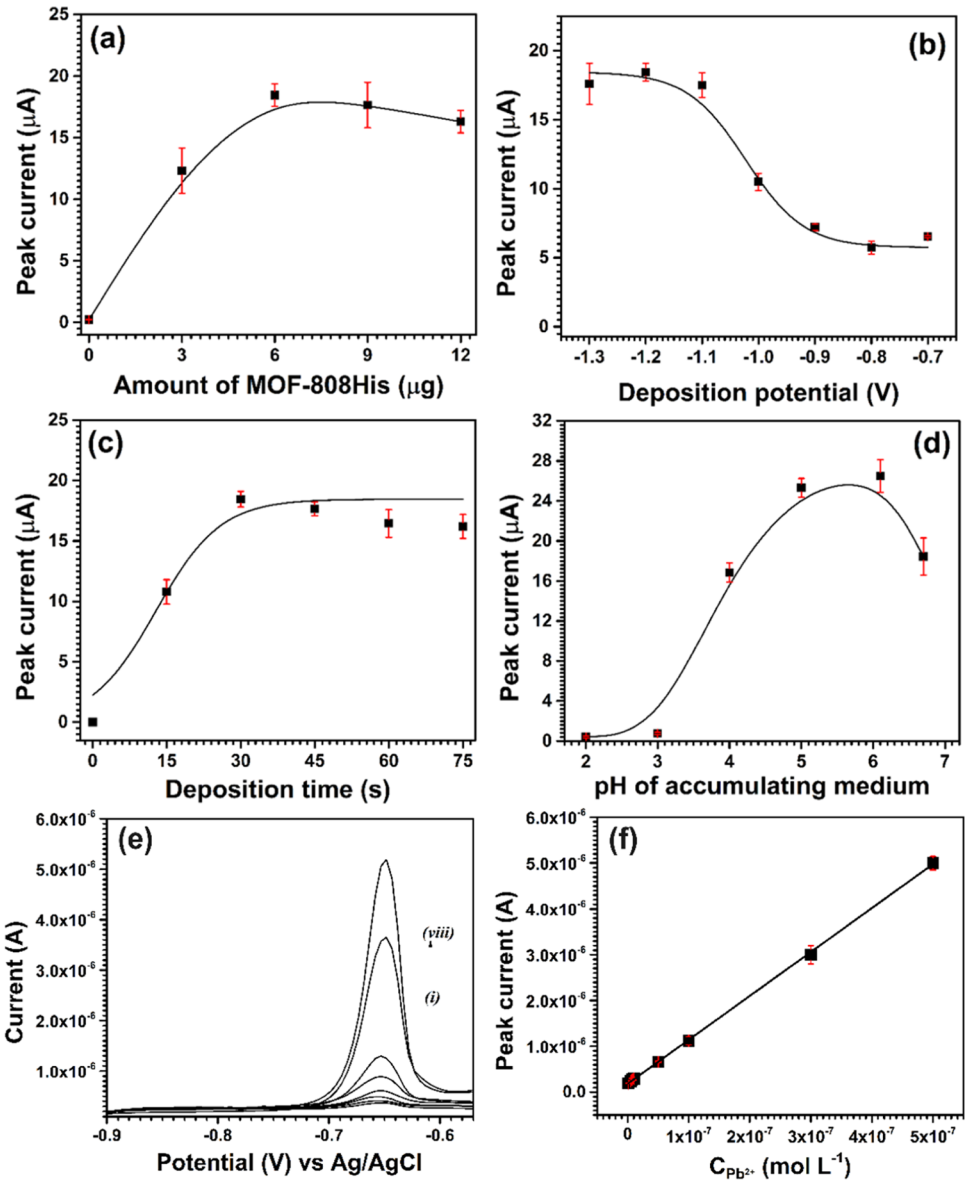

Figure 6. Optimization of experimental conditions. Amount of MOF-808-His on the electrode (a), deposition potential (b), deposition time (c), and influence of pH of accumulating medium (d), on the Pb^{2+} stripping current response on MOF-808-His/GCE. The experiments were run in triplicate, and the data points are an average of three repeated experiments (n = 3). (e) SWASV response of the MOF-808-His/GCE at different concentrations of Pb^{2+} ions at different concentrations: (i−viii): 0.001 and 0.5 μmol L^{-1} under optimal conditions and (f) calibration curve. Each data point is an average of three repeated experiments (n = 3).

The deposition potential was studied between −1.3 and −0.7 V. As illustrated in Figure 6b, the peak current of Pb^{2+} exhibited a pronounced and relatively stable magnitude within the potential range of −1.3 to −1.1 V, followed by a gradual decline at more positive potentials. This behavior can be attributed to the diminishing energy required for the reduction of Pb^{2+} ions. A deposition potential of −1.2 V was chosen for further experiments. The influence of deposition time on the peak current of 10 μmol L^{-1} Pb^{2+} at MOF-808-His/GCE after 1 min of preconcentration was assessed, and the corresponding outcomes are presented in Figure 6c. The current signals exhibited an initial rise within the 0 to 30 s time frame, followed by a subsequent attainment of a plateau.

After considering factors such as time consumption, sensitivity, and saturation of the working electrode, a deposition time of 30 s was selected for subsequent analyses.

It is worth noting that the pH of the solution significantly impacts the adsorption behavior of metal ions. As shown in Figure 6d, the peak current associated with the reduction of Pb^{2+} increases with pH values up to 5. The weak currents in acidic medium (pH up to 5.0) are due to the protonation (amine groups of His) of the MOF-808-His material which decreases the binding efficiency of Pb^{2+} due to protonation. On the other hand, between pH 5.0 and 6.1, the strongest relative peaks obtained are due to the easy adsorption of the lead monohydroxide complex $Pb(OH)^{+}$. Continued elevation of the pH (from 6.1 to 6.7) resulted in a decrease in the peak current. Within this specific pH range, the predominant formation of hydroxide complexes of lead, particularly $Pb(OH)^{-}$ and $Pb(OH)_2$, occurs primarily due to hydrolysis reactions.[58] pH 6.1 was chosen for further experiments.

https://doi.org/10.1021/acsami.3c15931
ACS Appl. Mater. Interfaces 2024, 16, 2509−2521

The relationship between the peak current and the accumulation time, as well as the concentration of the detection medium (HCl) containing 10 μmol L^{-1} Pb^{2+}, was investigated, and the findings are illustrated in Figure S9 (Supporting Information). In Figure S9a (Supporting Information), the electrode response increased progressively with accumulation time between 1 and 20 min; no saturation was reached and demonstrating a linear accumulation with time toward the end of the tested time interval. This behavior highlights many binding sites in the MOF-808-His material. An accumulation time of 10 min was chosen for subsequent experiments, as it represents an optimal trade-off between achieving high sensitivity and conducting rapid analyses. Figure S9b (Supporting Information) presents the effect of the detection medium concentration on the peak current of Pb^{2+} ions. Given that hydrochloric acid facilitates the desorption of accumulated complexes, the concentration range of 0.1 to 2.5 mol L^{-1} was optimized. It was observed that the detection of Pb^{2+} ions reached quantitative levels within the 1 and 2.5 mol L^{-1} range. Therefore, a solution of 1 mol L^{-1} HCl was chosen as the detection medium for subsequent analyses. In summary, for the quantitative individual determination of Pb^{2+} ions in aqueous solutions, a 10 min accumulation period in an aqueous solution with a pH of 6.1 is recommended, followed by a detection step in a 1 mol L^{-1} HCl solution with a 30 s application of potential at −1.2 V.

3.3.3. Analytical Performance, Interference, and Practical Applications of the Electrochemical Sensor. The linearity and sensitivity of the concurrent determination of Pb^{2+} were examined using SWASV under optimized conditions. As depicted in Figure 6e, the voltammograms of Pb^{2+} obtained from SWASV fell within the range of 0.001 to 0.5 μmol L^{-1}. Within this concentration range, a noticeable increase in peak current was observed as the lead concentration increased. Based on these results, the calibration curve (Figure 6f) with the equation: I_{pa} $(A) = 1.8 \times 10^{-7} + 9.6 \times C_{Pb^{2+}}$ (mol L^{-1}) was obtained with excellent linearity (R = 0.997), indicating excellent quantitative performance. Limit of detection (LoD) and limit of quantification (LoQ) were determined using the formulas LoD = 3 S_b/m and LoQ = 10 S_b/m, where S_b represents the standard deviation of the blank and m represents the slope of the calibration curve.[59] LoD and LoQ were estimated to be $(1.12 \times 10^{-10} \pm 0.10 \times 10^{-10})$ mol L^{-1} ((23.2 ± 2.1) ng L^{-1}) and $(3.75 \times 10^{-10} \pm 0.31 \times 10^{-10})$ mol L^{-1} ((77.7 ± 6.4) ng L^{-1}) (Conc. ± SD, n = 3), respectively. Additionally, the method exhibited a sensitivity of (9.6 ± 0.1) μA L μmol^{-1} was obtained. The detection limit was much lower than those of the listed electrochemical sensors in Table S2 (Supporting Information). These findings demonstrate that the developed electrochemical sensor exhibits a remarkable capacity to detect lead ions with notable sensitivity.

Selectivity plays a crucial role in assessing the performance of a sensor. Thus, each of these carefully selected ions (Cd^{2+}, Cu^{2+}, Zn^{2+}, Cr^{3+}, Sn^{2+}, Mn^{2+}, Ni^{2+}, Ag^{+}, Mg^{2+}, In^{3+}, Tm^{5+}, and Fe^{3+}) was intentionally introduced at the same concentration as Pb^{2+} and measured under optimal experimental conditions. The results obtained are summarized in Figure S10 (Supporting Information). The presence of Cd^{2+}, Cr^{3+}, Mg^{2+}, and Tm^{5+} was observed to have minimal impact on the signal of Pb^{2+} ions. However, a decrease in the recovery rate of Pb^{2+} ions was observed when Cu^{2+}, Zn^{2+}, Mn^{2+}, and Ni^{2+} were added due to their good affinity for the protonated amine groups on MOF-808-His. Similar behavior was observed for Sn^{2+}, Ag^{+}, In^{3+}, and Fe^{3+}. In^{3+} interfered with Pb^{2+} signal due to similar electrochemical behavior and stripping characteristics. Consequently, the presence of Sn^{2+}, Ag^{+}, In^{3+}, and Fe^{3+} in the same solution limited the selectivity of the proposed method.

This strong influence of metal ions on the determination of Pb^{2+} ions is also due to the difference in the stability constant of metal complexes involving sulfur and nitrogen atoms. Metal complexes based on cadmium with sulfur and nitrogen donor ligands, for example, show reduced stability (average $\log K$ = 4.6) compared with those based on lead (av. $\log K$ = 12.1).[60−62] The stability of copper complexes (av. $\log K$ = 12.5) is close to that of lead complexes. Therefore, it is recommended to completely remove these species, possibly through complexation, from any sample prior to Pb^{2+} detection. Notably, Na^{+}, K^{+}, Cl^{-}, SO_4^{2-}, and NO_3^{-}, which were not included in Figure S10 (Supporting Information), did not interfere with the Pb^{2+} signal.

Disinfection byproducts (DBPs) are widely acknowledged in potable water due to their cytotoxic, genotoxic, and carcinogenic properties.[63] DBPs, namely, 1,2-dichloromethane (DCM) and trifluoroacetic acid (TFAA) were, therefore, examined to verify the selectivity of the MOF-808-His sensor. Figure S10 (Supporting Information) shows that these two compounds increase the peak current of Pb^{2+} ions compared with other metal cations. TFAA can bind Pb^{2+} via its acetate functions, thereby increasing the metal ion concentration and consequently the peak current.

The stability of the electrochemical sensor was assessed by examining the current responses of the Pb^{2+} ions after the electrode had been stored for 1 week at a temperature of 4 °C and the results are shown in Figure S11a (Supporting Information). The current signal showed a recovery of 93.6%. The decrease in sensitivity can be attributed to material consumption during the sensing protocol and the structural deterioration of the MOF-808-His during the storage period. The sensor is reusable. Yet, this feature was evaluated after desorption in an acid medium. Acidic media can attenuate complexes formed between Pb^{2+} ions and histidine chelating groups. As shown in Figure S11b (Supporting Information), the same modified electrode was used 3 times for the determination of 10 μM Pb^{2+} under optimal conditions. The attenuation rates of the second and third analyses, relative to the first analysis, were determined to be 96.1 and 90.1%, respectively. These results mean that the MOF-808-His/GCE exhibits commendable cyclic and reusable characteristics in the current operating environment.

To assess the reproducibility of MOF-808-His/GCE, an intra-assay was conducted. Six MOF-808-His/GCE were prepared using the same procedures and utilized for the determination of 10 μmol L^{-1} Pb^{2+} (Experimental conditions: 0.1 mol L^{-1} HCl; deposition potential, −1.2 V; deposition time, 30 s; and accumulation time, 1 min) (Figure S12 in the Supporting Information) derived from the six electrodes for Pb^{2+} determination was 3.75%, indicating that the developed MOF-808-His-modified GCE had excellent reproducibility and stability for Pb^{2+} determination, which made it promising for practical applications in environmental lead ion monitoring. The suitability of MOF-808-His/GCE as a sensing platform for monitoring the quality of drinking water was assessed for the detection of minute quantities of lead in a tap water sample. Several concentrations were selected for the tap water examination, including a concentration lower than the WHO-prescribed value of 48 nmol L^{-1} (10 μg L^{-1}). The

https://doi.org/10.1021/acsami.3c15931
ACS Appl. Mater. Interfaces 2024, 16, 2509−2521

Pb^{2+} concentrations ascertained using the modified MOF-808-His/GCE were computed and presented in Table S3 (Supporting Information). The recovery acquired from the tap water sample in Pb^{2+} solutions of 20, 100, and 10,000 nmol L^{-1} were 94.5, 96.2, and 95.65%, respectively, indicating the significant potential of the proposed electrochemical sensor for practical implementations.

4. CONCLUSIONS

A modified electrode using a histidine-grafted metal−organic framework (MOF-808-His) was synthesized and applied for the detection of Pb^{2+} ions in aqueous solution. Due to its large specific surface area, high concentration of lead-binding sites, porosity, and electrical charge, MOF-808-His is useful for analyte accumulation and detection. The proposed sensor has a linearity region with a lower limit of $(1.12 \times 10^{-10} \pm 0.10 \times 10^{-10})$ mol L^{-1} and a sensitivity of (9.6 ± 0.1) μA μmol^{-1} L, which is significantly better than the reported analogues for electrochemical determination of lead. The practical usability of our proposed method was validated by testing the lead determination in tap water, i.e., in the presence of typical interfering ions, where less than 10 μmol L^{-1} Pb^{2+} were detectable. Thereby a simple, sensitive, and reliable electrochemical sensor based on a highly porous MOF material is proposed as a sensor model for environmental monitoring.

■ ASSOCIATED CONTENT

Supporting Information

The Supporting Information is available free of charge at https://pubs.acs.org/doi/10.1021/acsami.3c15931.

> Energy-dispersive X-ray spectroscopy (EDS) element mappings; ^{1}H NMR analysis of histidine; ^{1}H NMR analysis of MOF-808, ^{1}H NMR analysis of MOF-808-His; elemental analysis; TG analysis; assessment of electrochemical sensing capabilities for $[Fe(CN)_6]^{3-}$ ions at pH 3; assessment of electrochemical sensing capabilities for $[Ru(NH_3)_6]^{3+}$ ions at pH 3; CV curves at various scan rates (10 to 150 mV s^{-1}) recorded in 0.1 mol L^{-1} $NaNO_3$ containing 0.5 mmol L^{-1} $[Fe(CN)_6]^{3-}$; dependence of the peak current on the accumulation time and the concentration of detection medium; comparison of the performance of some electrochemical sensors and analytical methods for determining Pb^{2+} ions; interference studies; stability and reusability tests; reproducibility of lead signal on MOF-808-His/GCE sensor; and application of the sensor MOF-808-His/GCE to tap water (PDF)

■ AUTHOR INFORMATION

Corresponding Authors

Sherman Lesly Zambou Jiokeng − *Institut für Anorganische Chemie und Strukturchemie, Heinrich-Heine-Universität Düsseldorf, 40204 Düsseldorf, Germany; Electrochemistry and Chemistry of Materials, Department of Chemistry, University of Dschang, 00237 Dschang, Cameroon;* orcid.org/0000-0002-3279-8139; Email: sherman.jiokeng@univ-dschang.org

Christoph Janiak − *Institut für Anorganische Chemie und Strukturchemie, Heinrich-Heine-Universität Düsseldorf, 40204 Düsseldorf, Germany;* orcid.org/0000-0002-6288-9605; Email: janiak@uni-duesseldorf.de

Authors

Tobie J. Matemb Ma Ntep − *Institut für Anorganische Chemie und Strukturchemie, Heinrich-Heine-Universität Düsseldorf, 40204 Düsseldorf, Germany*

Marcus N. A. Fetzer − *Institut für Anorganische Chemie und Strukturchemie, Heinrich-Heine-Universität Düsseldorf, 40204 Düsseldorf, Germany*

Till Strothmann − *Institut für Anorganische Chemie und Strukturchemie, Heinrich-Heine-Universität Düsseldorf, 40204 Düsseldorf, Germany;* orcid.org/0000-0001-7953-2699

Cyrille G. Fotsop − *Institute of Chemistry, Faculty of Process and Systems Engineering, 39106 Magdeburg, Germany;* orcid.org/0000-0001-6455-2515

Ignas Kenfack Tonle − *Electrochemistry and Chemistry of Materials, Department of Chemistry, University of Dschang, 00237 Dschang, Cameroon;* orcid.org/0000-0001-9794-788X

Complete contact information is available at: https://pubs.acs.org/10.1021/acsami.3c15931

Author Contributions

S.L.Z.J. synthesized materials, carried out characterization and electrochemical measurements, and wrote the manuscript. T.J.M.M.N. participated in powder X-ray diffraction measurements and material synthesis. M.N.A.F. performed scanning electron microscopy. C.G.F. EDS-elemental mapping analysis. T.S. carried out the thermogravimetric analysis. I.K.T. revised and edited the manuscript. C.J. supervised, provided resources, proofread, and refined the manuscript. All authors have given approval to the final version of the manuscript.

Notes

The authors declare no competing financial interest.

■ ACKNOWLEDGMENTS

S.L.Z.J. thanks the German Academic Exchange Service (DAAD) for financial support (grant number 57588366). C.J. thanks the Deutsche Forschungsgemeinschaft (DFG) within the Priority Program SPP 1928/2 COORNETs (grant Ja466/43-1). The authors thank Birgit Tommes for carrying out the FTIR experiments, and Ishtvan Boldog for his participation in the interpretation of the results of the thermogravimetric and ^{1}H NMR characterizations. The authors also thank the Centre for Molecular and Structural Analytics at Heinrich Heine University (CeMSA@HHU) for recording the NMR spectra.

■ REFERENCES

(1) Briffa, J.; Sinagra, E.; Blundell, R. Heavy Metal Pollution in the Environment and Their Toxicological Effects on Humans. *Heliyon* **2020**, *6*, No. e04691.

(2) Li, P.; Liu, B.; Zhang, D.; Sun, Y.; Liu, J. Graphene Field-Effect Transistors with Tunable Sensitivity for High Performance Hg(II) Sensing. *Appl. Phys. Lett.* **2016**, *109* (15), No. 153101.

(3) Li, P.; Zhang, D.; Jiang, C.; Zong, X.; Cao, Y. Ultra-Sensitive Suspended Atomically Thin-Layered Black Phosphorus Mercury Sensors. *Biosens. Bioelectron.* **2017**, *98*, 68−75.

(4) Zhou, G.; Xu, X.; Zhu, W.; Feng, B.; Hu, J. Dispersedly Embedded Loading of Fe_3O_4 Nanoparticles into Graphene Nanosheets for Highly Efficient and Recyclable Removal of Heavy Metal Ions. *New J. Chem.* **2015**, *39* (9), 7355−7362.

(5) Huang, K.; Li, B.; Zhou, F.; Mei, S.; Zhou, Y.; Jing, T. Selective Solid-Phase Extraction of Lead Ions in Water Samples Using Three-

Dimensional Ion-Imprinted Polymers. *Anal. Chem.* **2016**, *88* (13), 6820−6826.
(6) Jiokeng, S. L. Z.; Dongmo, L. M.; Ymélé, E.; Ngameni, E.; Tonlé, I. K. Sensitive Stripping Voltammetry Detection of Pb(II) at a Glassy Carbon Electrode Modified with an Amino-Functionalized Attapulgite. *Sens. Actuators, B* **2017**, *242*, 1027−1034.
(7) Hakonen, A.; Strömberg, N. Fluorescence and Naked-Eye Detection of Pb^{2+} in Drinking Water Using a Low-Cost Ionophore Based Sensing Scheme. *Chemosensors* **2018**, *6* (4), 51.
(8) Ru, J.; Wang, X.; Cui, X.; Wang, F.; Ji, H.; Du, X.; Lu, X. GaOOH-Modified Metal-Organic Frameworks UiO-66-NH_2: Selective and Sensitive Sensing Four Heavy-Metal Ions in Real Wastewater by Electrochemical Method. *Talanta* **2021**, *234*, No. 122679.
(9) Awual, M. R.; Hasan, M. M.; Shahat, A. Functionalized Novel Mesoporous Adsorbent for Selective Lead(II) Ions Monitoring and Removal from Wastewater. *Sens. Actuators, B* **2014**, *203*, 854−863.
(10) Liang, L.; Lan, F.; Ge, S.; Yu, J.; Ren, N.; Yan, M. Metal-Enhanced Ratiometric Fluorescence/Naked Eye Bimodal Biosensor for Lead Ions Analysis with Bifunctional Nanocomposite Probes. *Anal. Chem.* **2017**, *89* (6), 3597−3605.
(11) Saha, D.; Barakat, S.; van Bramer, S. E.; Nelson, K. A.; Hensley, D. K.; Chen, J. Noncompetitive and Competitive Adsorption of Heavy Metals in Sulfur-Functionalized Ordered Mesoporous Carbon. *ACS Appl. Mater. Interfaces* **2016**, *8* (49), 34132−34142.
(12) Mo, J.; Zhou, L.; Li, X.; Li, Q.; Wang, L.; Wang, Z. On-Line Separation and Preconcentration on a Mesoporous Silica-Grafted Graphene Oxide Adsorbent Coupled with Solution Cathode Glow Discharge-Atomic Emission Spectrometry for the Determination of Lead. *Microchem. J.* **2017**, *130*, 353−359.
(13) Wan, Z.; Xu, Z.; Wang, J. Flow Injection On-Line Solid Phase Extraction for Ultra-Trace Lead Screening with Hydride Generation Atomic Fluorescence Spectrometry. *Analyst* **2006**, *131* (1), 141−147.
(14) Ji, L.; Guo, Y.; Hong, S.; Wang, Z.; Wang, K.; Chen, X.; Zhang, J.; Hu, J.; Pei, R. Label-Free Detection of Pb^{2+} Based on Aggregation-Induced Emission Enhancement of Au-Nanoclusters. *RSC Adv.* **2015**, *5* (46), 36582−36586.
(15) Shaily; Kumar, A.; Parveen, I.; Ahmed, N. Highly Selective and Sensitive Coumarin−Triazole-Based Fluorometric 'Turn-off' Sensor for Detection of Pb^{2+} Ions. *Luminescence* **2018**, *33* (4), 713−721.
(16) Hsieh, H. F.; Chang, W. S.; Hsieh, Y. K.; Wang, C. F. Lead Determination in Whole Blood by Laser Ablation Coupled with Inductively Coupled Plasma Mass Spectrometry. *Talanta* **2009**, *79* (2), 183−188.
(17) Choi, H. W.; Lee, K. H.; Hur, N. H.; Lim, H. B. Cerium Oxide-Deposited Mesoporous Silica Nanoparticles for the Determination of Carcinoembryonic Antigen in Serum Using Inductively Coupled Plasma-Mass Spectrometry. *Anal. Chim. Acta* **2014**, *847*, 10−15.
(18) Jin, J. C.; Wu, J.; Yang, G. P.; Wu, Y. L.; Wang, Y. Y. A Microporous Anionic Metal−Organic Framework for a Highly Selective and Sensitive Electrochemical Sensor of Cu^{2+} Ions. *Chem. Commun.* **2016**, *52* (54), 8475−8478.
(19) Yang, Z.; Huang, X.; Zhang, R.; Li, J.; Xu, Q.; Hu, X. Novel Urchin-like In_2O_3−Chitosan Modified Electrode for Direct Electrochemistry of Glucose Oxidase and Biosensing. *Electrochim. Acta* **2012**, *70*, 325−330.
(20) Jiokeng, S. L. Z.; Dongmo, L. M.; Ymélé, E.; Nde, D. B.; Tonlé, I. K. Organoclay-Film Modified Electrode for the Detection of Ultra-Traces of Hg^{2+} Ions: Approach of One Factor at a Time by an Experimental Design. *Electrochim. Acta* **2019**, *316*, 152−161.
(21) Guenang, L. S.; Dongmo, L. M.; Jiokeng, S. L. Z.; Kamdem, A. T.; Doungmo, G.; Tonlé, I. K.; Bassetto, V. C.; Jović, M.; Lesch, A.; Girault, H. Montmorillonite Clay-Modified Disposable InkJet-Printed Graphene Electrode as a Sensitive Voltammetric Sensor for the Determination of Cadmium(II) and Lead(II). *SN Appl. Sci.* **2020**, *2* (3), No. 476, DOI: 10.1007/s42452-020-2283-5.
(22) Ngassa, G. B. P.; Tonlé, I. K.; Walcarius, A.; Ngameni, E. One-Step Co-Intercalation of Cetyltrimethylammonium and Thiourea in Smectite and Application of the Organoclay to the Sensitive Electrochemical Detection of Pb(II). *Appl. Clay Sci.* **2014**, *99*, 297−305.
(23) Pecheu, C. N.; Jiokeng, S. L. Z.; Tamo, A. K.; Doungmo, G.; Doench, I.; Osorio-Madrazo, A.; Tonlé, I. K.; Ngameni, E. Fabrication of an Organofunctionalized Talc-like Magnesium Phyllosilicate for the Electrochemical Sensing of Lead Ions in Water Samples. *Nanomaterials* **2022**, *12* (17), 2928.
(24) Xuan, X.; Park, J. Y. A Miniaturized and Flexible Cadmium and Lead Ion Detection Sensor Based on Micro-Patterned Reduced Graphene Oxide/Carbon Nanotube/Bismuth Composite Electrodes. *Sens. Actuators, B* **2018**, *255*, 1220−1227.
(25) Wang, Y.; Wu, Y.; Xie, J.; Hu, X. Metal−Organic Framework Modified Carbon Paste Electrode for Lead Sensor. *Sens. Actuators, B* **2013**, *177*, 1161−1166.
(26) Ding, Y.; Wei, F.; Dong, C.; Li, J.; Zhang, C.; Han, X. UiO-66 Based Electrochemical Sensor for Simultaneous Detection of Cd(II) and Pb(II). *Inorg. Chem. Commun.* **2021**, *131*, No. 108785.
(27) Lu, M.; Deng, Y.; Luo, Y.; Lv, J.; Li, T.; Xu, J.; Chen, S. W.; Wang, J. Graphene Aerogel-Metal-Organic Framework-Based Electrochemical Method for Simultaneous Detection of Multiple Heavy-Metal Ions. *Anal. Chem.* **2019**, *91* (1), 888−895.
(28) Sun, X.; Chen, Y.; Xie, Y.; Wang, L.; Wang, Y.; Hu, X. Preparation of a Chemically Stable Metal−Organic Framework and Multi-Walled Carbon Nanotube Composite as a High-Performance Electrocatalyst for the Detection of Lead. *Analyst* **2020**, *145* (5), 1833−1840.
(29) Liu, L.; Zhou, Y.; Liu, S.; Xu, M. The Applications of Metal−Organic Frameworks in Electrochemical Sensors. *ChemElectroChem* **2018**, *5* (1), 6−19.
(30) Pournara, A. D.; Tarlas, G. D.; Papaefstathiou, G. S.; Manos, M. J. Chemically Modified Electrodes with MOFs for the Determination of Inorganic and Organic Analytes via Voltammetric Techniques: A Critical Review. *Inorg. Chem. Front.* **2019**, *6* (12), 3440−3455.
(31) Howarth, A. J.; Katz, M. J.; Wang, T. C.; Platero-Prats, A. E.; Chapman, K. W.; Hupp, J. T.; Farha, O. K. High Efficiency Adsorption and Removal of Selenate and Selenite from Water Using Metal-Organic Frameworks. *J. Am. Chem. Soc.* **2015**, *137* (23), 7488−7494.
(32) Desai, A. V.; Manna, B.; Karmakar, A.; Sahu, A.; Ghosh, S. K. A Water-Stable Cationic Metal−Organic Framework as a Dual Adsorbent of Oxoanion Pollutants. *Angew. Chem.* **2016**, *128* (27), 7942−7946.
(33) Lustig, W. P.; Mukherjee, S.; Rudd, N. D.; Desai, A. V.; Li, J.; Ghosh, S. K. Metal−Organic Frameworks: Functional Luminescent and Photonic Materials for Sensing Applications. *Chem. Soc. Rev.* **2017**, *46* (11), 3242−3285.
(34) Wu, M. X.; Yang, Y. W. Metal−Organic Framework (MOF)-Based Drug/Cargo Delivery and Cancer Therapy. *Adv. Mater.* **2017**, *29* (23), No. 1606134.
(35) Zhao, Y.; Zhang, Y.; Liu, A.; Wei, Z.; Liu, S. Construction of Three-Dimensional Hemin-Functionalized Graphene Hydrogel with High Mechanical Stability and Adsorption Capacity for Enhancing Photodegradation of Methylene Blue. *ACS Appl. Mater. Interfaces* **2017**, *9* (4), 4006−4014.
(36) Zuluaga, S.; Fuentes-Fernandez, E. M. A.; Tan, K.; Xu, F.; Li, J.; Chabal, Y. J.; Thonhauser, T. Understanding and Controlling Water Stability of MOF-74. *J. Mater. Chem. A* **2016**, *4* (14), 5176−5183.
(37) Wang, Y.; Wang, L.; Huang, W.; Zhang, T.; Hu, X.; Perman, J. A.; Ma, S. A Metal−Organic Framework and Conducting Polymer Based Electrochemical Sensor for High Performance Cadmium Ion Detection. *J. Mater. Chem. A* **2017**, *5* (18), 8385−8393.
(38) Baek, J.; Rungtaweevoranit, B.; Pei, X.; Park, M.; Fakra, S. C.; Liu, Y. S.; Matheu, R.; Alshmimri, S. A.; Alshehri, S.; Trickett, C. A.; Somorjai, G. A.; Yaghi, O. M. Bioinspired Metal-Organic Framework Catalysts for Selective Methane Oxidation to Methanol. *J. Am. Chem. Soc.* **2018**, *140* (51), 18208−18216.
(39) Fang, X.; Zong, B.; Mao, S. Metal−Organic Framework-Based Sensors for Environmental Contaminant Sensing. *Nano-Micro Lett.* **2018**, *10* (4), No. 64.

(40) Cui, L.; Wu, J.; Li, J.; Ju, H. Electrochemical Sensor for Lead Cation Sensitized with a DNA Functionalized Porphyrinic Metal-Organic Framework. *Anal. Chem.* **2015**, *87* (20), 10635−10641.
(41) Xu, Z.; Yang, L.; Xu, C. Pt@UiO-66 Heterostructures for Highly Selective Detection of Hydrogen Peroxide with an Extended Linear Range. *Anal. Chem.* **2015**, *87* (6), 3438−3444.
(42) Zeng, Z.; Fang, X.; Miao, W.; Liu, Y.; Maiyalagan, T.; Mao, S. Electrochemically Sensing of Trichloroacetic Acid with Iron(II) Phthalocyanine and Zn-Based Metal Organic Framework Nanocomposites. *ACS Sens.* **2019**, *4*, 1934−1941.
(43) Moll, B.; Müller, T.; Schlüsener, C.; Schmitz, A.; Brandt, P.; Öztürk, S.; Janiak, C. Modulated Synthesis of Thiol-Functionalized Fcu and Hcp UiO-66(Zr) for the Removal of Silver(I) Ions from Water. *Mater. Adv.* **2021**, *2* (2), 804−812.
(44) Chen, X.; Liu, Y.; Fang, X.; Li, Q.; Zeng, Z.; Maiyalagan, T.; Mao, S. Nanocomposites of Zr(IV)-Based Metal-Organic Frameworks and Reduced Graphene Oxide for Electrochemically Sensing Ciprofloxacin in Water Nanocomposites of Zr(IV)-Based Metal−Organic Frameworks and Reduced Graphene Oxide for Electrochemically Sensing Ciprofloxacin in Water. *ACS Appl. Nano Mater.* **2019**, *2*, 2367−2376.
(45) Furukawa, H.; Gándara, F.; Zhang, Y. B.; Jiang, J.; Queen, W. L.; Hudson, M. R.; Yaghi, O. M. Water Adsorption in Porous Metal-Organic Frameworks and Related Materials. *J. Am. Chem. Soc.* **2014**, *136* (11), 4369−4381.
(46) Sindoro, M.; Yanai, N.; Jee, A. Y.; Granick, S. Colloidal-Sized Metal-Organic Frameworks: Synthesis and Applications. *Acc. Chem. Res.* **2014**, *47* (2), 459−469.
(47) Lyu, H.; Chen, O. I. F.; Hanikel, N.; Hossain, M. I.; Flaig, R. W.; Pei, X.; Amin, A.; Doherty, M. D.; Impastato, R. K.; Glover, T. G.; Moore, D. R.; Yaghi, O. M. Carbon Dioxide Capture Chemistry of Amino Acid Functionalized Metal-Organic Frameworks in Humid Flue Gas. *J. Am. Chem. Soc.* **2022**, *144* (5), 2387−2396.
(48) Jiang, J.; Gándara, F.; Zhang, Y. B.; Na, K.; Yaghi, O. M.; Klemperer, W. G. Superacidity in Sulfated Metal-Organic Framework-808. *J. Am. Chem. Soc.* **2014**, *136* (37), 12844−12847.
(49) van Velthoven, N.; Henrion, M.; Dallenes, J.; Krajnc, A.; Bugaev, A. L.; Liu, P.; Bals, S.; Soldatov, Av.; Mali, G.; de Vos, D. E. S,O-Functionalized Metal-Organic Frameworks as Heterogeneous Single-Site Catalysts for the Oxidative Alkenylation of Arenes via C-H Activation. *ACS Catal.* **2020**, *10* (9), 5077−5085.
(50) Reinsch, H.; Waitschat, S.; Chavan, S. M.; Lillerud, K. P.; Stock, N. A Facile "Green" Route for Scalable Batch Production and Continuous Synthesis of Zirconium MOFs. *Eur. J. Inorg. Chem.* **2016**, *2016*, 4490−4498.
(51) Zhu, Z.; Zhang, P.; Li, B.; Chen, S.; Deng, Q.; Zeng, Z.; Wang, J.; Deng, S. Chemical Immobilization of Amino Acids into Robust Metal−Organic Framework for Efficient SO_2 Removal. *AIChE J.* **2021**, *67* (9), No. e17300.
(52) Liu, S.; Zhang, Y.; Meng, Y.; Gao, F.; Jiao, S.; Ke, Y. Fast Syntheses of MOFs Using Nanosized Zeolite Crystal Seeds in Situ Generated from Microsized Zeolites. *Cryst. Growth Des.* **2013**, *13* (7), 2697−2702.
(53) Trickett, C. A.; Gagnon, K. J.; Lee, S.; Gándara, F.; Bürgi, H. B.; Yaghi, O. M. Definitive Molecular Level Characterization of Defects in UiO-66 Crystals. *Angew. Chem., Int. Ed.* **2015**, *54* (38), 11162−11167.
(54) Bohigues, B.; Rojas-Buzo, S.; Moliner, M.; Corma, A. Coordinatively Unsaturated Hf-MOF-808 Prepared via Hydrothermal Synthesis as a Bifunctional Catalyst for the Tandem N-Alkylation of Amines with Benzyl Alcohol. *ACS Sustainable Chem. Eng.* **2021**, *9* (47), 15793−15806.
(55) Marcus, Y. Ionic Radii in Aqueous Solutions. *Chem. Rev.* **1988**, *88*, 1475−1498.
(56) Fernandes, D. M.; Silva, N.; Pereira, C.; Moura, C.; Magalhães, J. M. C. S.; Bachiller-Baeza, B.; Rodríguez-Ramos, I.; Guerrero-Ruiz, A.; Delerue-Matos, C.; Freire, C. $MnFe_2O_4$@CNT-N as Novel Electrochemical Nanosensor for Determination of Caffeine, Acetaminophen and Ascorbic Acid. *Sens. Actuators, B* **2015**, *218*, 128−136.
(57) Martin Santos, A.; Wong, A.; Araújo Almeida, A.; Fatibello-Filho, O. Simultaneous Determination of Paracetamol and Ciprofloxacin in Biological Fluid Samples Using a Glassy Carbon Electrode Modified with Graphene Oxide and Nickel Oxide Nanoparticles. *Talanta* **2017**, *174*, 610−618.
(58) Bouwe, R. G. B.; Tonlé, I. K.; Letaief, S.; Ngameni, E.; Detellier, C. Structural Characterisation of 1,10-Phenanthroline−Montmorillonite Intercalation Compounds and Their Application as Low-Cost Electrochemical Sensors for Pb(II) Detection at the Sub-Nanomolar Level. *Appl. Clay Sci.* **2011**, *52* (3), 258−265.
(59) Ghoneim, M. M.; Hassanein, A. M.; Hammam, E.; Beltagi, A. M. Simultaneous Determination of Cd, Pb, Cu, Sb, Bi, Se, Zn, Mn, Ni, Co and Fe in Water Samples by Differential Pulse Stripping Voltammetry at a Hanging Mercury Drop Electrode. *Fresenius J. Anal. Chem.* **2000**, *367* (4), 378−383.
(60) Cesarino, I.; Cavalheiro, T. G.; Brett, C. M. A. Simultaneous Determination of Cadmium, Lead, Copper and Mercury Ions Using Organofunctionalized SBA-15 Nanostructured Silica Modified Graphite-Polyurethane Composite Electrode. *Electroanalysis* **2010**, *22* (1), 61−68.
(61) Pellissier, A.; Bretonnière, Y.; Chatterton, N.; Pécaut, J.; Delangle, P.; Mazzanti, M. Relating Structural and Thermodynamic Effects of the Pb(II) Lone Pair: A New Picolinate Ligand Designed to Accommodate the Pb(II) Lone Pair Leads to High Stability and Selectivity. *Inorg. Chem.* **2007**, *46* (9), 3714−3725.
(62) Al-Kandary, J. A.; Mandani, F. M. A.; Al-Jimaz, A. S.; El-Sherif, A. A.; Shoukry, M. M. Synthesis and Thermodynamic Investigation of 4-Amino-6-Hydroxy-2-Mercapto Pyrimidine (AHMP) Complexes with Some Selected Divalent Metal(II) Ions. *J. Solution Chem.* **2007**, *36* (2), 247−257.
(63) Richardson, S. D.; Plewa, M. J.; Wagner, E. D.; Schoeny, R.; Demarini, D. M. Occurrence, Genotoxicity, and Carcinogenicity of Regulated and Emerging Disinfection by-Products in Drinking Water: A Review and Roadmap for Research. *Mutat. Res.* **2007**, *636*, 178−242.

https://doi.org/10.1021/acsami.3c15931
ACS Appl. Mater. Interfaces 2024, 16, 2509−2521